PHYSICAL REVIEW A **82**, 053808 (2010)

Mechanism of high-energy pulse generation without wave breaking in mode-locked fiber lasers

Xueming Liu[*]
State Key Laboratory of Transient Optics and Photonics, Xi'an Institute of Optics and Precision Mechanics,
Chinese Academy of Sciences, Xi'an 710119, China

(Received 4 October 2010; published 10 November 2010)

The mechanism and intrinsic conditions of high-energy wave-breaking-free pulse generation in fiber lasers mode-locked by a nonlinear polarization rotation technique are investigated numerically and experimentally. Both numerical and experimental results show that the pulses along the two orthogonal polarization axes of the fiber have a large difference in pulse energy. The numerical simulations show that the ratio of the energy of two components is limited and ranges from about 8 to about 65. The slope of the instantaneous frequency at the central position of the pulse decreases rapidly with the increase of the pulse duration and energy, whereas the slope at the pulse edge changes slightly. The accumulation of instantaneous frequency throughout the pulse width approaches a constant in a higher pulse energy regime. Understanding the mechanism and intrinsic conditions of the wave-breaking-free pulse generation could be useful in generating high-energy pulses delivered from fiber lasers.

DOI: 10.1103/PhysRevA.82.053808 PACS number(s): 42.65.Tg, 42.55.Wd, 42.81.Dp, 42.65.Re

I. INTRODUCTION

High-energy fiber lasers can have widespread applications as practical alternatives to bulk solid-state lasers, offering compact size, simple design, high stability, low cost, and freedom from misalignment [1–6]. In the past decade, the major increases in the pulse energy have been achieved by adjusting the intracavity structure with the appropriate dispersion, including stretched-pulse lasers [4,7,8], parabolic-pulse lasers [1,9], and all-normal-dispersion lasers [5,10,11]. These techniques effectively decrease, but do not eliminate, the effects of nonlinearity through dispersion management.

The accumulation of excessive nonlinear phase shift or excessive pulse chirp often causes the pulse to break up and hence presents a fundamental challenge to the development of high-energy fiber lasers [5,6]. Direct management of the nonlinearity of the laser cavity has been proposed for substantial increases in pulse energy [12]. Ilday *et al.* [12] showed that a linear anomalous-dispersion segment suppresses wave-breaking effects of solitonlike pulse shaping at high energies. Ruehl *et al.* [3] proposed a hybrid mode-locking scheme for wave-breaking-free fiber lasers based on a saturable Bragg reflector and the nonlinear polarization evolution in the fiber section. Tian *et al.* [13] and Li *et al.* [2] experimentally demonstrated an all-fiber mode-locked laser system which generated high-energy wave-breaking-free pulses in the normal and anomalous dispersion regimes. Chang *et al.* [14] proposed a dissipative soliton resonance technique to achieve high-energy pulses, and this technique could be operated in the anomalous- and normal-dispersion regimes [15,16].

Anderson *et al.* proved that wave breaking can be avoided when a pulse acquires a monotonic frequency sweep or chirp as it propagates [17]. Until now, however, the mechanism of why the mode-locked fiber lasers deliver the wave-breaking-free pulses has not been uncovered completely. In our previous report, we proposed a strongly dissipative-dispersive fiber laser delivering high-energy wave-breaking-free pulses [18]. What are the mechanism and intrinsic conditions that preserve the pulse evolution without wave breaking? This work answers this question. Understanding this issue will be useful in generating high-energy pulses delivered from fiber lasers.

II. NUMERICAL MODEL

The lightwave propagation in the weakly birefringent fibers is modeled by the two coupled nonlinear Schrödinger equations that involve a vector electric field [19,20]. When the total cavity length L (here $L > 25$ m) is far longer than the beat length L_B of fiber (usually $L_B \approx 1$ m), the coupled equations can ignore the terms related to the four-wave mixing [18,19]. Then the coupled equations are expressed by

$$\begin{aligned}\frac{\partial u}{\partial z} &= -\frac{\alpha}{2}u - \delta\frac{\partial u}{\partial T} - i\frac{\beta_2}{2}\frac{\partial^2 u}{\partial T^2} + i\gamma\left(|u|^2 + \frac{2}{3}|v|^2\right)u \\ &\quad + \frac{g}{2}u + \frac{g}{2\Omega_g^2}\frac{\partial^2 u}{\partial T^2}, \\ \frac{\partial v}{\partial z} &= -\frac{\alpha}{2}v + \delta\frac{\partial v}{\partial T} - i\frac{\beta_2}{2}\frac{\partial^2 v}{\partial T^2} + i\gamma\left(|v|^2 + \frac{2}{3}|u|^2\right)v \\ &\quad + \frac{g}{2}v + \frac{g}{2\Omega_g^2}\frac{\partial^2 v}{\partial T^2}. \qquad (1)\end{aligned}$$

Here u and v are the envelopes of the optical pulses along the two orthogonal polarization axes of the fiber. Conveniently, we define u and v to be S and P components of the electric field, respectively. The variables T and z denote the time and the propagation distance, respectively. α, δ, β_2, γ, and Ω_g are the loss coefficient of fiber, the group velocity difference between the two polarization modes, the fiber dispersion, the cubic refractive nonlinearity of the medium, and the bandwidth of the laser gain, respectively. The net gain g describes the gain function of doped fiber and is expressed by $g = g_0 \exp(-E_p/E_s)$ [21], where g_0, E_s, and E_p are the small-signal gain, the gain saturation energy, and the pulse energy, respectively. E_s corresponds to the pumping strength [22,23]. When the soliton propagates through the polarization additive pulse mode-locking (P-APM) element, the intensity

---

[*] liuxueming72@yahoo. com

transmission, T_i, is expressed as

$$T_i = \sin^2(\theta)\sin^2(\varphi) + \cos^2(\theta)\cos^2(\varphi) + 0.5\sin(2\theta)\sin(2\varphi)\cos(\phi_1 + \phi_2), \qquad (2)$$

where ϕ_1 is the phase delay caused by the polarization controllers and ϕ_2 is the phase delay resulting from the fiber including both the linear phase delay and the nonlinear phase delay. The polarizer and the analyzer have orientation angles θ and φ with respect to the fast axis of the fiber, respectively (see Fig. 6).

III. SIMULATION RESULTS

Equation (1) is numerically solved with a predictor-corrector split-step Fourier method [24]. In simulations, we use the following parameters for possibly matching the experimental conditions: $\alpha = 0.2\,\mathrm{dB/km}$, $g_0 = 2\,\mathrm{m}^{-1}$, $\Omega_g = 30\,\mathrm{nm}$, $\phi_1 = 0.25 + \pi/2$, $\gamma = 4.5\ \mathrm{W}^{-1}\ \mathrm{km}^{-1}$ and $\beta_2 = 55\ \mathrm{ps}^2/\mathrm{km}$ for doped gain fiber, and $\gamma = 1.3\ \mathrm{W}^{-1}\ \mathrm{km}^{-1}$ and $\beta_2 = -22\ \mathrm{ps}^2/\mathrm{km}$ for undoped fiber. The length of doped and undoped fibers is 18 and 7.5 m, respectively. On the basis of the aforementioned parameters, the numerical model describing the mode-locked fiber lasers is simulated. Figure 1 shows the domain of existence of wave-breaking-free pulse solutions as a function of orientation angles θ and φ normalized by π. Figures 1(b) and 1(c) are the local view of the bottom-left and top-left portions of Fig. 1(a), respectively. The color regions in Fig. 1 illustrate the domain of existing wave-breaking-free pulse solutions, but white regions show the domain of existence of multiple pulses or the instability operation. It can be found from Fig. 1 that the wave-breaking-free pulse solutions exist in the range from $\varphi \approx 0.039\pi$ to 0.111π. The report in Ref. [25] demonstrates a typical example of fiber lasers operating on the multiple pulses at $\varphi = 0.2\pi$. The contour lines with numbers in Figs. 1(b) and 1(c) denote the ratio R_P of the peak power of S and P components (an example is shown in Fig. 2).

Numerical results show that, to achieve wave-breaking-free pulse solutions, the ratio R_P must be more than about 8 and simultaneously be less than about 65. Figure 1 demonstrates an example of numerical simulations. One can observe from Fig. 1 that R_P is approximately independent of the orientation angle θ and increases with the decrease of φ.

Figure 2 illustrates the profiles of S and P components in an example with $E_s = 16$ nJ, $\theta = 0.25\pi$, and $\varphi = 0.1\pi$, where (a) and (b) denote the temporal and spectral profiles of the wave-breaking-free pulse solutions, respectively. It can be found from Fig. 2 that the ratio R_P of the peak power of S and P components is about 9.5 in this example and the energy ratio of the two components of the pulse also is about 9.5. The numerical results show that R_P approximately is the same as the ratio of energy of S and P components.

Because fibers have weak birefringence, the S and P components travel along the fiber at different speeds. The "walk-off" effect that originates from the birefringence of fiber then leads to the pulse becoming broader [19]. The ratio R_P at the wave-breaking-free pulse solution region is more than about 8 (Fig. 1). Physically speaking, the component of the pulse moving along one of the two orthogonal polarization axes of the fiber is much more intense than that moving along the other axis. The pulse approximates a linearly polarized wave propagating along the fiber. The P component can be dealt with by a small perturbation on the S component and this appears to be an "asymmetric" combined pulse state with one pulse component being much smaller than the other [26]. Then the pulse broadening induced by the walk-off effect can be effectively avoided, as can the prevention of pulses from wave breaking. On the other hand, when R_P is more than about 65, the nonlinear polarization rotation effect is

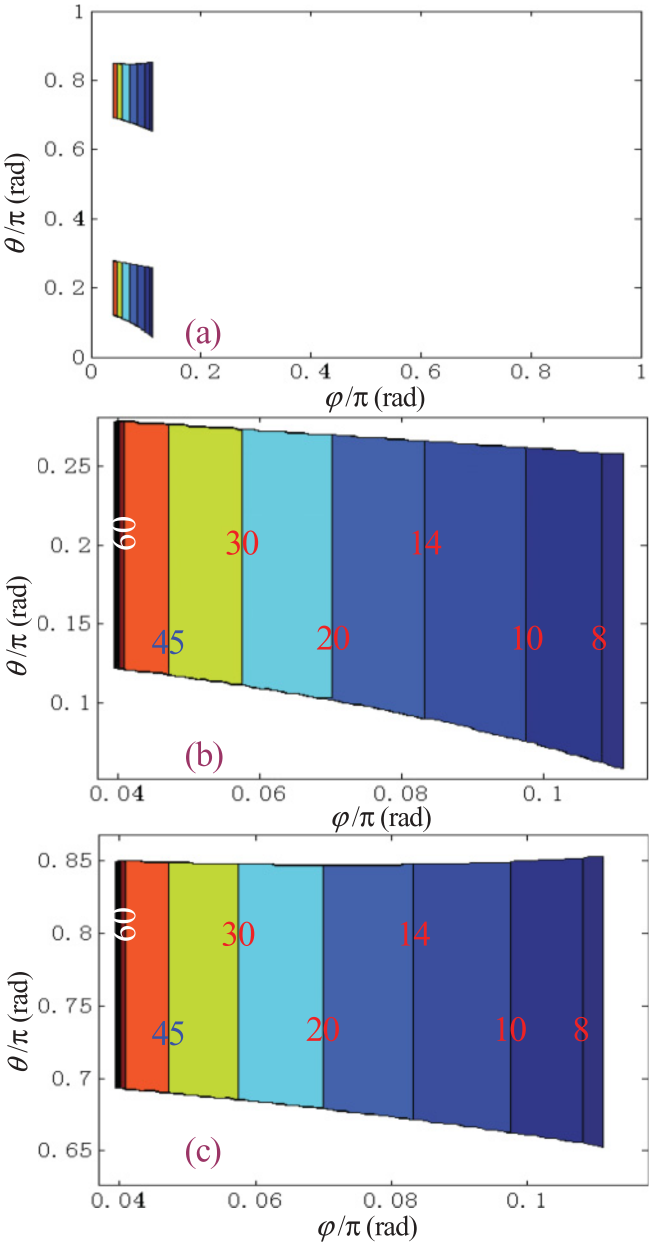

FIG. 1. (Color online) (a) Domain of existence of wave-breaking-free pulse solutions of fiber lasers as a function of orientation angles θ and φ normalized by π. (b) Zoomed in view of the bottom-left portion of panel (a). (c) Zoomed in view of the top-left portion of panel (a). Color regions, wave-breaking-free pulses exist; white regions, multiple pulses or instability operattion. The contour lines with numbers in panels (b) and (c) denote the ratio R_P of the peak power of S and P components.

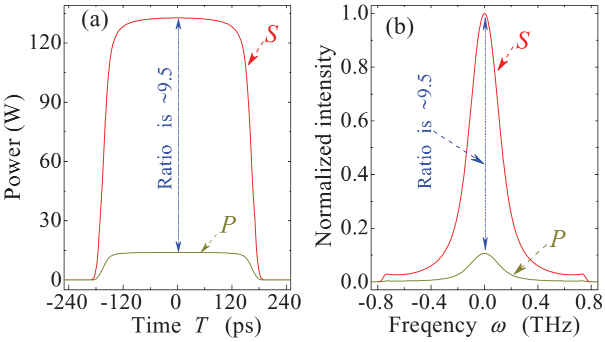

FIG. 2. (Color online) (a) Temporal and (b) spectral profiles of S and P components of pulse in the example of $E_s = 16$ nJ, $\theta = 0.25\pi$, and $\varphi = 0.1\pi$. The ratio R_P of the peak power (intensity) of S and P components is about 9.5. The ratio of energy of two components also is about 9.5.

disabled because the pulse energy of a component of the two orthogonal polarization axes of the fiber is far more intense than that of the other component. The nonlinear polarization rotation technique fails to mode-lock lasers at this state. By adjusting the length and dispersion of the intracavity, numerical simulations show that R_P of S and P components is approximately confined with a lower limit of about 8 and an upper limit of about 65. Of course, the lower and upper limits of R_P have slight fluctuation for lasers with different intracavity lengths and dispersions. Therefore, the range of R_P from about 8 to about 65 is one of the intrinsic conditions that preserve the pulse evolution without wave breaking.

Figures 3(a) and 3(b) show the temporal power profile and the instantaneous frequency $\delta\omega$ of the pulses at $E_s = 16$ nJ, $\theta = 0.25\pi$, and $\varphi = 0.1\pi$. One can easily find from Fig. 3(b) that the instantaneous frequency $\delta\omega$ is nearly linear across the central region of the pulse whereas it is nonlinear at the edges of the pulse. We define S_1 and S_2 to be the slopes of $\delta\omega$ at the central position $T = 0$ and at the pulse edge located at half maximum [Fig. 3(b)]. From Figs. 3(a) and 3(b), we can find the pulse duration $\Delta\tau \approx 325$ ps, $S_1 \approx 0.012$ THz/ps, and $S_2 \approx 0.264$ THz/ps. Obviously, S_1 is far less than S_2.

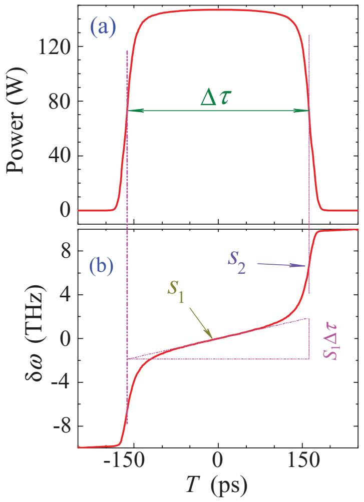

FIG. 3. (Color online) (a) Temporal power profile and (b) instantaneous frequency $\delta\omega$ of the pulses at $E_s = 16$ nJ. $\Delta\tau$ is the pulse duration. S_1 and S_2 are the slopes of $\delta\omega$ at the central position $T = 0$ and at the pulse edge located at half maximum. $S_1\Delta\tau$ denotes the accumulation of instantaneous frequency $\delta\omega$ throughout the pulse width $\Delta\tau$.

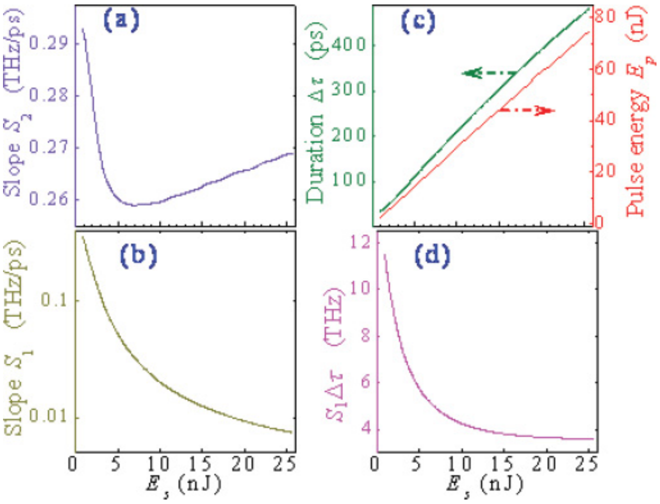

FIG. 4. (Color online) Evolutions of (a) S_2, (b) S_1, (c) the pulse duration $\Delta\tau$ and energy E_p, and (d) the product of S_1 and the pulse duration $\Delta\tau$, $S_1\Delta\tau$, as a function of pumping strength E_s, respectively. $S_1\Delta\tau$ approximately approaches 3.6 THz for $E_s > 20$ nJ.

Figures 4(a)–4(d) illustrate the evolutions of S_2, S_1, the pulse duration $\Delta\tau$ and energy E_p, and the product $S_1\Delta\tau$ as a function of pumping strength E_s, respectively. It is found that S_1 exponentially decreases along E_s [Fig. 4(b)], whereas S_2 approximately tends to a constant of about 0.27 THz/ps [Fig. 4(a)]. For $E_s = 25$ nJ, $S_1 \approx 0.0076$ THz/ps is over 35 times less than $S_2 \approx 0.2687$ THz/ps. With the increase of E_s, therefore, the slope of instantaneous frequency $\delta\omega$ at $T = 0$ decreases rapidly but the slope of $\delta\omega$ at the edges are fixed approximately. So the frequency changes nonlinearly across the pulse; that is, the nonlinear frequency chirp is imposed on the pulse.

Figure 4(c) shows that the pulse duration $\Delta\tau$ and energy E_p approximately linearly increase along E_s with the fit line functions $\Delta\tau = 18.5E_s + 20.8$ and $E_p = 2.9E_s - 0.15$, respectively. The evolution of pulse profiles is similar to Fig. 2 of Ref. [18]. Figure 4(d) illustrates that the product of S_1 and $\Delta\tau$, $S_1\Delta\tau$, decreases in the beginning of E_s and then approaches a constant of 3.6 THz. From a physical point of view, the product $S_1\Delta\tau$ represents the accumulation of frequency $\delta\omega$ throughout the pulse width. The graphical interpretation for the product $S_1\Delta\tau$ is shown in Fig. 3(b).

By changing $\varphi = \pi/11$, $\varphi = \pi/12$, and $\pi/13$, the evolution of $S_1\Delta\tau$ is shown in Fig. 5, respectively. One can find from Fig. 5 that, although the ratio R_P of two components is so different, the product $S_1\Delta\tau$ changes slightly. For example, when φ decreases from $\pi/10$ to $\pi/13$, R_P increases about 2 times from about 9.5 to 16.5, whereas $S_1\Delta\tau$ only changes from 3.6 to 3.9. We can find from Figs. 4(c), 4(d), and 5 that, under a fixed φ, the product $S_1\Delta\tau$ approaches a constant in the higher pumping strength regime (e.g., $E_s > 20$ nJ) although the pulse duration and energy linearly increase from about 300 ps and 50 nJ. Therefore, although the pulse duration and

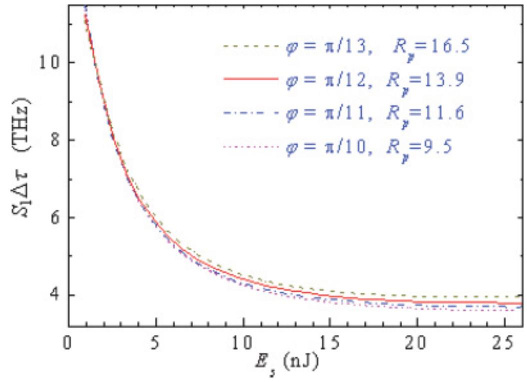

FIG. 5. (Color online) Evolutions of the product $S_1\Delta\tau$ as a function of pumping strength E_s. The parameters used are the same as those used in Fig. 4, except for φ. For $\varphi = \pi/10, \pi/11, \pi/12$, and $\pi/13$, the ratio R_P is about 9.5, 11.6, 13.9, and 16.5, respectively, and $S_1\Delta\tau$ tends to about 3.6, 3.7, 3.8, and 3.9 THz for $E_s > 20$ nJ from bottom to top, respectively.

energy increases as a function of pumping strength E_s, the slope S_1 of $\delta\omega$ at the central position $T = 0$ decreases and the accumulation of instantaneous frequency tends to a constant.

Physically speaking, the wave-breaking-free pulses have very-low-frequency chirps across the central region of pulses for higher pulse energy operation. Since different frequency components of a pulse travel at different speeds along the laser system [19], very-low-frequency chirps mean that the frequency components of the pulse travel at approximately the same speed. Meanwhile, the nonlinear chirp of the pulse edge can effectively withstand the influence of normal dispersion that incurs the linear chirp to pulses. As a result, the dispersion-induced pulse broadening can be extremely weakened.

Therefore, a very-low-frequency chirp in the central region of the pulse, together with the nonlinear chirp at the edge of the pulse, is another intrinsic condition that preserves the pulse in a wave-breaking-free operation in a high-energy regime. The numerical results prove that the accumulation of the frequency chirp throughout the pulse width approximates the constant (Fig. 5). This theoretical prediction is in good agreement with the result reported in dissipative soliton resonance [15].

IV. EXPERIMENTAL SETUP AND RESULTS

The fiber laser is schematically shown in Fig. 6. The ring cavity is made of a polarization-sensitive isolator (PS-ISO), two sets of polarization controllers (PCs), a fused coupler with 50% output, two sets of wavelength-division multiplexing (WDM) couplers, an 18-m-long erbium-doped fiber (EDF) with absorption of 6 dB/m at 980 nm, and a segment of standard single-mode fiber. EDF provides the gain amplification for the laser system pumped by two 977-nm laser diodes (LDs). To increase the pumping strength, the laser is pumped bidirectionally rather than unidirectionally. The parameters are the same as the numerical simulations. A polarization beam splitter (PBS) is used to separate the two orthogonal polarizations of the laser emission, and S and P components are simultaneously measured with an optical spectrum analyzer (Yokogawa AQ-6370) and a 70-GHz digital

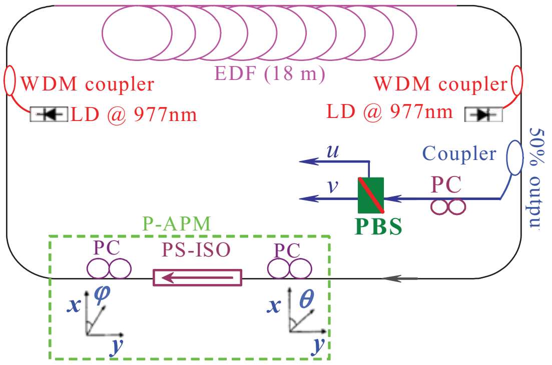

FIG. 6. (Color online) Schematic diagram of the experimental setup for the proposed laser. EDF, erbium-doped fiber; WDM, wavelength-division multiplexing; PC, polarization controller; PS-ISO, polarization-sensitive isolator; PBS, polarization beam splitter; P-APM, polarization additive pulse mode-locking; LD, laser diode.

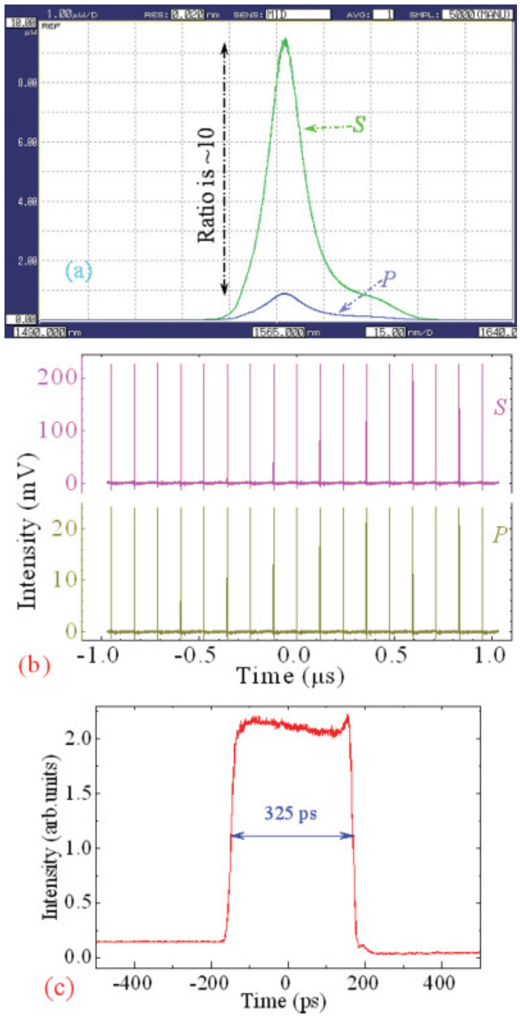

FIG. 7. (Color online) (a) Output spectra and (b) oscilloscope traces for S and P components. (c) Single-pulse profile. Pulses were measured with a Tektronix TDS8200 digital sampling oscilloscope. Both the forward and backward pump powers are 500 mW. The ratios of the peak power (intensity) of the S and P components for optical spectra and oscilloscope traces are about 10 and 9.4, respectively.

sampling oscilloscope (Tektronix TDS8200) together with a 50-GHz photodetector.

With appropriate orientation and pressure settings of the polarization controllers, mode-locking self starts at the forward pump power of about 100 mW with a fundamental repetition rate of about 8 MHz (corresponding to about 0.125 μs, [Fig. 7(b)]). The experimental observations show that the single-pulse operation is always maintained in the laser and the pulse duration increases from about 60 to 340 ps as the pump power is gradually enhanced. When the forward and backward pump powers are both 500 mW, the output spectra and the oscilloscope traces are as illustrated in Fig. 7. Figure 7(a) shows that the optical spectra of pulses are similar to the Gaussian profile, centered at about 1568 nm, with full width at half maximum about 13 nm. The ratio of the peak values of S and P components for optical spectra is about 10. The pedestal of optical spectra at the longer wavelength in Fig. 7(a) originates from the amplified spontaneous emission of the erbium-doped fiber.

Figure 7(b) shows the oscilloscope traces of the S and P components within 17 round-trips. The intensity peak of the S component is about 230 mV, which is about 9.4 times larger than that of the P component [Fig. 7(b)]. Since the measured pulse height in the oscilloscope trace is directly related to the energy of each individual pulse, the ratio of the energy of the S and P components of the pulse is about 9.4. The difference between the ratio of the intensity in the spectral domain [Fig. 7(a)] and that in the temporal domain [Fig. 7(b)] comes from the fact that the photodetector works at the saturation state for higher intensity. Figure 7(c) exhibits the pulse profiles with a pulse duration of about 325 ps.

By comparing Fig. 7 to Figs. 2 and 3, the experimental observations are in good agreement with the theoretical predictions. For instance, the pulse duration is about 325 ps for theoretical and experimental results [Figs. 3(a) and 7(c)], the pulses have Gaussian spectral profiles [Figs. 2(b) and 7(a)] and quasirectangular temporal profiles [Figs. 3(a) and 7(c)], and the ratio of the S and P components is about 9.5 [Figs. 2, 7(a), and 7(b)].

V. CONCLUSIONS

We have numerically and experimentally investigated the mechanism and intrinsic conditions of high-energy wave-breaking-free pulse generation in fiber lasers mode-locked by a nonlinear polarization rotation technique. The theoretical predictions and experimental observations show that the energy of the pulses along one of the two orthogonal polarization axes of the fiber is very different from that along the other axis. The energy ratio of two components of the pulse is limited in range from about 8 to about 65. With the increase of the pulse duration and energy, the slope S_1 of the instantaneous frequency $\delta\omega$ at the central position of pulse decreases rapidly, whereas the slope S_2 of $\delta\omega$ at the pulse edge varies slightly. The product of S_1 and pulse duration $\Delta\tau$, $S_1\Delta\tau$, approaches a constant in the higher pulse energy regime; that is, the accumulation of the frequency chirp of the pulse throughout the pulse width approximates a constant. Understanding the mechanisms and intrinsic conditions of the wave-breaking-free pulse generation could be useful in generating high-energy pulses delivered from fiber lasers.

ACKNOWLEDGMENTS

This work was supported by the National Natural Science Foundation of China under Grants No. 10874239 and No. 10604066. The author would especially like to thank Dong Mao, Leiran Wang, and Lina Duan for help with the experiments.

---

[1] F. O. Ilday, J. R. Buckley, W. G. Clark, and F. W. Wise, Phys. Rev. Lett. **92**, 213902 (2004).
[2] X. H. Li, X. Liu, X. Hu, L. Wang, H. Lu, Y. Wang, and W. Zhao, Opt. Lett. **35**, 3249 (2010).
[3] A. Ruehl, D. Wandt, U. Morgner, and D. Kracht, Opt. Express **16**, 8181 (2008).
[4] K. Tamura, E. P. Ippen, H. A. Haus, and L. E. Nelson, Opt. Lett. **18**, 1080 (1993).
[5] F. W. Wise, A. Chong, and W. Renninger, Laser Photonics Rev. **2**, 58 (2008).
[6] X. Liu, L. Wang, X. Li, H. Sun, A. Lin, K. Lu, Y. Wang, and W. Zhao, Opt. Express **17**, 8506 (2009).
[7] V. Roy, M. Olivier, F. Babin, and M. Piche, Phys. Rev. Lett. **94**, 203903 (2005).
[8] M. Salhi, H. Leblond, and F. Sanchez, Phys. Rev. A **68**, 033815 (2003).
[9] B. Bale and J. Kutz, Phys. Rev. E **79**, 046602 (2009).
[10] A. Chong, J. Buckley, W. Renninger, and F. Wise, Opt. Express **14**, 10095 (2006).
[11] W. H. Renninger, A. Chong, and F. W. Wise, Phys. Rev. A **77**, 023814 (2008).
[12] F. O. Ilday, J. Buckley, H. Lim, F. Wise, and W. Clark, Opt. Lett. **28**, 1365 (2003).
[13] X. Tian, M. Tang, X. Cheng, P. Shum, Y. Gong, and C. Lin, Opt. Express **17**, 7222 (2009).
[14] W. Chang, A. Ankiewicz, J. M. Soto-Crespo, and N. Akhmediev, J. Opt. Soc. Am. B **25**, 1972 (2008).
[15] W. Chang, A. Ankiewicz, J. M. Soto-Crespo, and N. Akhmediev, Phys. Rev. A **78**, 023830 (2008).
[16] W. Chang, J. M. Soto-Crespo, A. Ankiewicz, and N. Akhmediev, Phys. Rev. A **79**, 033840 (2009).
[17] D. Anderson, M. Desaix, M. Karlsson, M. Lisak, and M. L. Quiroga-Teixeiro, J. Opt. Soc. Am. B **10**, 1185 (1993).
[18] X. Liu, Phys. Rev. A **81**, 053819 (2010).
[19] G. P. Agrawal, *Nonlinear Fiber Optics*, 4th ed. (Academic Press, Boston, 2007).
[20] C. R. Menyuk, IEEE J. Quantum Electron. **25**, 2674 (1989).
[21] G. Agrawal, IEEE Photonics Technol. Lett. **2**, 875 (1990).
[22] A. Cabasse, B. Ortac, G. Martel, A. Hideur, and J. Limpert, Opt. Express **16**, 19322 (2008).
[23] G. Martel, C. Chedot, V. Reglier, A. Hideur, B. Ortac, and P. Grelu, Opt. Lett. **32**, 343 (2007).
[24] X. M. Liu and B. Lee, IEEE Photonics Technol. Lett. **15**, 1549 (2003).
[25] X. Liu, Phys. Rev. A **81**, 023811 (2010).
[26] N. Akhmediev and J. M. Soto-Crespo, Phys. Rev. E **49**, 4519. (1994).